

Modelling and experiment of vibro-impact vibration energy harvester based on a partial interlayer-separated piezoelectric beam

Dong-Xing Cao^{1,2}, Wei Xia^{1,3}, Xiang-Ying Guo^{*1,2}, Siu-Kai Lai⁴

¹ College of Mechanical Engineering, Beijing University of Technology, Beijing 100124, China;

² Beijing Key Laboratory of Nonlinear Vibrations and Strength of Mechanical Structures, Beijing 100124, China;

³ China Aerospace Science and Industry Corporation Limited Institute of Magnetic Levitation and Electromagnetic Propulsion, Beijing 100143, China

⁴ Department of Civil and Environmental Engineering, The Hong Kong Polytechnic University, Hung Hom, Kowloon, Hong Kong, China

*Corresponding author:

Xiang-Ying Guo, College of Mechanical Engineering, Beijing University of Technology, Beijing 100124, China

Email: eagle2008guo@yeah.net

Abstract

Piezoelectric-based energy harvesting techniques offer a promising way to transform vibration energy into electric energy. However, many vibration energy harvesters (VEH) can only work under narrow bandwidths and limited high frequencies to restrict their working performance. In this paper, a vibro-impact piezoelectric VEH is proposed, where a partial interlayer-separated piezoelectric beam is designed to improve the voltage output and frequency bandwidth of the VEH. First, the mechanism of the proposed VEH is introduced and the electromechanical model is derived based on the Euler-Bernoulli beam theory and vibro-impact dynamic model. Voltage-frequency responses are then obtained by using an approximate analytical method. In addition, the effect of partial interlayer-separated piezoelectric beams on the energy harvesting performance is investigated numerically. A parametric study is performed to investigate the influence of system parameters on the voltage output in terms of bandwidth and magnitude. Finally, the theoretical solutions are validated by experimental results, the voltage output of the proposed VEH is higher than the non-impact type. The maximum output power of the proposed VEH is about 12 times more than that of the conventional one under a 0.2g acceleration. Due to the good agreement of the variation trend between the theoretical values and experiment results, the proposed partial interlayer-separated beam VEH can be used for a further optimization of the vibration energy harvester.

Keywords: Vibration energy harvesting; Partial interlayer-separated piezoelectric beam; Vibro-impact; Low-frequency vibration; Wide bandwidth

1. Introduction

For micro-electronic devices and systems, chemical batteries are traditionally used as a power supply. However, the lifespan of batteries is limited and the replacement is rather frequent and difficult. Exploring new energy sources for micro-electronics has aroused great interests in fundamental research and practical implications. With the rapid development of wireless sensors, energy harvesting techniques are viable solutions to capture energy from the ambient environment to autonomously supply power to micro-electronics (Ando et al., 2010).

Among various electromechanical conversion principles, such as electrostatic, electromagnetic and piezoelectric approaches, piezoelectric-based vibration energy harvesting techniques are one of the major approaches to convert mechanical energy to electrical energy due to its power density, stability and integration (Erturk and Inman, 2011; Daqaq et al., 2014; Zou et al., 2019). Making use of piezoelectric-based vibration energy harvesting techniques, one of the most critical issues is to match wider frequency bands under disorganized external excitation. Hence, many studies have devoted to investigate various piezoelectric-based models to improve the conversion efficiency, such as bi-stable (Andò et al., 2013; Erturk et al., 2009; Sun and Cao, 2017; Lan et al., 2015), multi-stable (Zhou et al., 2014; Zhou and Zuo, 2018; Lai et al., 2019), multi-degree (Yuan et al., 2018; Zhao et al., 2018b; Fan et al., 2019) and variable stiffness beam models (Cao et al., 2019a; Cao et al., 2019b; Hajhosseini and Rafeeyan, 2016; Lee et al., 2009). There are also some studies to investigate various types of VEH under stochastic excitations (Liu et al., 2017a; Liu et al., 2017b; Xu et al., 2014), flow-induced vibration (Wang et al., 2020; Wang et al., 2019; Cao et al., 2020a; Cao et al., 2020b) and nonlinear internal resonance (Cao et al., 2015; Lu et al., 2019; Jiang et al., 2016).

Vibro-impact occurs in many engineering applications and vibro-impact dynamics has been analyzed extensively in many literatures. In recent years, vibro-impact models were introduced to vibration energy harvesters to improve the harvesting efficiency. Halim *et al.* (Halim et al., 2016; Halim and Park, 2014) presented piezoelectric-based energy harvesters with a stopper-engaged dynamic magnifier that can be able to increase the operating bandwidth. Gu (Gu, 2011) designed a low-frequency VEH based on periodic impact motions for energy harvesting. Zhou *et al.* (Zhou et al., 2015) applied the shock-induced method to convert low-frequency excitation to high-frequency vibration. Kim *et al.* (Kim et al., 2016) fabricated a spring-supported piezoelectric cantilever beam that can work under the impact of a free-fall ball at the tip. Dechant *et al.* (Dechant et al., 2017) also proposed a

percussive VEH to convert mechanical energy under low-frequency excitation into electrical energy. Moss *et al.* (Moss et al., 2010) demonstrated a vibro-impacting approach to construct a relatively broadband kinetic energy harvester. Fu *et al.* (Fu et al., 2018; Fu et al., 2019) presented a vibration energy harvester through triboelectric and electrostatic effects from the vibro-impact of multi-degree mechanical system. In addition, some other studies (Hu et al., 2017; Liu et al., 2016; Zhao et al., 2018a; Hu et al., 2018) proposed various two-degree-of-freedom piecewise-linear piezoelectric VEHs to achieve wide frequency bandwidths. Results show that the performance of vibration-based energy harvesters can be effectively enhanced by mechanical impact model. Fang et al. (Fang et al., 2019) designed an asymmetric plucking-based bistable energy harvester with rotary structure and plectrum and used Hertzian contact theory to analyze the different oscillation modes with dynamic plucking force under variations of plucking velocity and overlap length. Furthermore, Fang *et al.* (Fang et al., 2020) proposed a rotational impact energy harvester, which applied the advantages of the centrifugal softening effect to improve the impact energy harvesting performance at low rotational frequencies. Xie *et al.* (Xie et al., 2019) proposed an impact-bistable piezoelectric energy harvester and demonstrated the advantages of both the bistable system and impact-based excitation.

In general, the vibro-impact VEH systems usually consist of flexible beams and relatively rigid stoppers. Moreover, magnets are also introduced to reduce the natural frequencies of the system. Numerous literatures have already demonstrated the advantages of the vibro-impact VEH from wide bandwidth and lower frequency excitation. However, conventional vibro-impact VEHs need much more space to assemble the driving system, impactor or magnet, that is disadvantageous to expand the engineering applications especially for the integration with micro-electro-mechanical system. In order to overcome these issues, the authors (Cao et al., 2019c) proposed a layer-separated vibration energy harvester based on vibro-impact model, where there is no need any other impactor. The results show that it's realizable to scavenge the vibration energy. However, it is easy to find that the length of the completely interlayer-separated piezoelectric beam has to be smaller, otherwise the vibration response will be complicated because of the elastic rigidity of the separated piezoelectric layer (PVDF material). Hence, in this paper, a partial interlayer-separated piezoelectric beam is designed for a vibro-impact driving VEH.

The paper is organized as follows. First, the configuration and the working mechanism of the harvester are introduced in Section 2, where a theoretical model is constructed. Analytical solutions for this model are presented in Section 3. Numerical simulations are

performed to investigate the effect of different parameters on the frequency bandwidth and output power of the system in Section 4. Experimental results for the harvester are provided in Section 5. Finally, concluding remarks are given.

2. Configuration of the proposed device

The proposed piezoelectric energy harvester is made up of a piezoelectric laminated cantilever beam with a tip mass at the free end, where the beam consists of a protective layer, a piezoelectric layer and a fundamental layer. The piezoelectric layer is made of polyvinylidene fluoride (PVDF) sheet for energy conversion. The fundamental and protective layers are made of brass and polyester sheets, respectively. Figs.1(a) and (b) demonstrate the prototype and the dynamic model of the proposed vibro-impact VEH. The special design of this structure is that the piezoelectric and fundamental layers are separated partially at the free end. Considering the smaller partial separation, the upper separated segment, that includes the separated piezoelectric and protective parts, and the original tip mass are integrated as a spring-damper-mass oscillator, as shown in Fig. 1(b). Furthermore, it is assumed that the mass of the separated fundamental segment is smaller than that of the upper separated segment and the unseparated part, so here, the mass of the separated fundamental segment is ignored. Meanwhile, due to the stiffness of the lower separated fundamental layer is larger than the upper layer, the lower separated segment, with the separated fundamental layer, is regarded as a massless spring-damper stopper in this paper.

In detail, the parameters, k and c are the stiffness and damping of the lower separated segment, respectively, while k_2 and c_2 are the stiffness and damping of the upper separated segment. d is the gap distance between the end of the two layers. L and L_2 are the length of overlapped part and the separated part of the partial interlayer-separated piezoelectric beam, respectively. The lumped mass of the integrated upper separated segment is defined as $m = 33m_u/140 + m_t$, where m_t and m_u are the tip mass and the total mass of the upper separated layer, respectively.

The geometry of the cross-section of the overlapped part for the partial interlayer-separated piezoelectric beam is shown in Fig. 1(c). The width of the piezoelectric beam is b . The thickness of the piezoelectric layer, fundamental layer and protective layer are h_p , h_b and h_s , respectively. Hence, the cross-sectional areas of these three layers are $A_p = bh_p$, $A_b = bh_b$ and $A_s = bh_s$, respectively. Their densities are ρ_p , ρ_b and ρ_s , and the Young's modulus are C_{xx}^E , E_b and E_s , respectively.

When a sinusoidal excitation with amplitude A and frequency ω , $z(t) = A\sin(\omega t)$, is imposed on the beam, it will vibrate and vibro-impact will occur between the upper and lower separated parts. Hence, power generation can be measured due to the deformation of the piezoelectric beam.

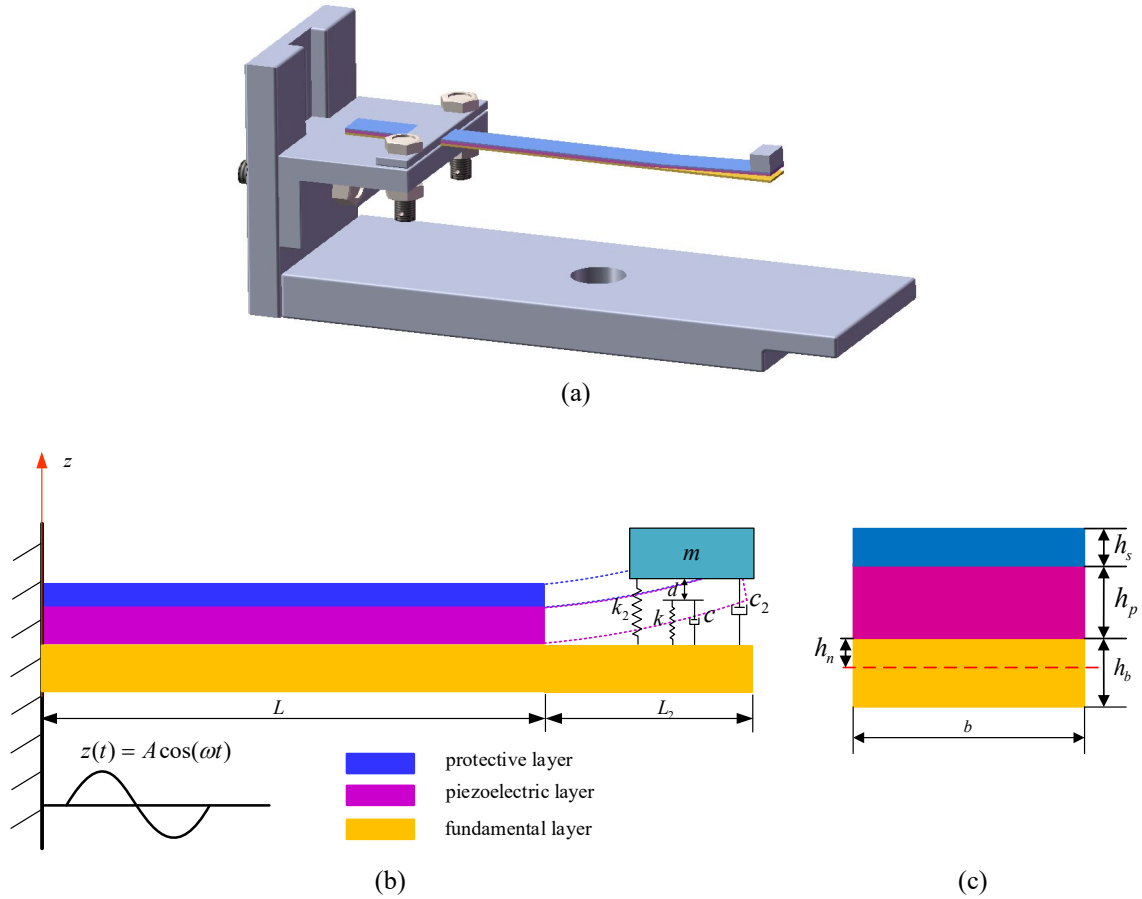


Fig.1 Mechanical configuration of the proposed vibro-impact VEH: (a) the prototype model; (b) the dynamic model; (c) cross section of the overlapped beam

3. Theoretical modeling and formulation

3.1 Governing equations

For theoretical analysis, the following assumptions are taken into consideration to derive the governing equation: (a) the impact between the separated parts occurs only at the free end of the piezoelectric and fundamental layers; (b) the sectional plane of the overlapped part is still perpendicular to the mid-plane after transverse bending; (c) the moment of inertia is neglected; (d) only the transverse electric field is considered; (e) only the vertical vibration of the lumped mass is considered; and (f) the separated and overlapped parts of the upper layer can be viewed as two independent generators, and the total output of the system is the summation of the output voltage of these parts.

The x -axis of the mechanical model is located on the neutral layer of the overlapped

part that can be obtained as follows:

$$h_n = \frac{E_b h_b^2 - 4C_{xx}^E [h_p - (C_{xx}^E h_p^2 - E_s h_s^2)/2(C_{xx}^E h_p + E_s h_s)]^2}{2E_b h_b + 4C_{xx}^E [h_p - (C_{xx}^E h_p^2 - E_s h_s^2)/2(C_{xx}^E h_p + E_s h_s)]} \quad (1)$$

Based on the electromechanical coupling model, the following linear constitutive equations are used to calculate the potential energy of the piezoelectric layer of the overlapped part

$$T_x = C_{xx}^E S_x - d_{zx} E_z \quad (2a)$$

$$D_z = d_{zx} S_x + \varepsilon_{zz}^S E_z \quad (2b)$$

where T_x and S_x are the stress and strain along the length of the piezoelectric layer, respectively. D_z is the electric displacement, E_z is the electric field induced on the piezoelectric layer, d_{zx} is the piezoelectric strain coefficient and ε_{zz}^S is the laminate permittivity.

The kinetic energy of the system is expressed as follows:

$$T = \frac{1}{2} (\rho_p A_p + \rho_s A_s + \rho_b A_b) \int_0^L \dot{u}^2 dx + \frac{1}{2} m \dot{w}^2 \quad (3)$$

where u is the transverse displacement of the overlapped part of the composite beam, w is the transverse displacement of the lumped mass

$$u(x, t) = v(x, t) + z(t) \quad (4a)$$

$$w(t) = s(t) + v(L, t) + z(t) \quad (4b)$$

where $v(x, t)$ is the relative displacement of the overlapped part, $s(t)$ is the displacement of the lumped mass relative to the free end of the overlapped part and $z(t)$ is the displacement of the base excitation.

The potential energy of the system is given as follows:

$$U = \frac{1}{2} \int_V T_x S_x dV - \frac{1}{2} \int_{V_p} D_z E_z dV_p + \frac{1}{2} k_2 (w - u_L)^2 + \frac{1}{2} k (w - u_L + d)^2 H - \theta_2 \dot{\lambda}_2 (w - u_L) + \frac{1}{2} C_{p2} \dot{\lambda}_2^2 \quad (5)$$

where C_{p2} , θ_2 and $\dot{\lambda}_2$ are the electric capacity, electromechanical coupling coefficient and voltage of the upper separate layer, respectively. u_L indicates the transverse displacement of the overlapped part at the separated point. And H is a piecewise function as follows:

$$H = \begin{cases} 0 & (w - u_L \geq -d) \\ 1 & (w - u_L < -d) \end{cases} \quad (6)$$

The virtual work of the system is expressed as follow:

$$\int_{t_0}^{t_1} \delta W dt = - \int_{t_0}^{t_1} \int_0^L c_0 \dot{v} \delta v dx dt - \int_{t_0}^{t_1} \frac{\dot{\lambda}_1}{R_{L1}} \delta \lambda_1 dt - \int_{t_0}^{t_1} c_2 (\dot{w} - \dot{u}_L) \delta (w - u_L) dt - \int_{t_0}^{t_1} c (\dot{w} - \dot{u}_L) H \delta (w - u_L) dt - \int_{t_0}^{t_1} \frac{\dot{\lambda}_2}{R_{L2}} \delta \lambda_2 dt \quad (7)$$

where c_0 is damping of the unit length of the overlapped part, and $\dot{\lambda}_1$ is the voltage of the overlapped part. The relationship between $\dot{\lambda}_1$ and E_z is

$$E_z = - \frac{\dot{\lambda}_1}{h_p} \quad (8)$$

The nonlinear strain and transversal displacement of the overlapped part is given as follows:

$$\varepsilon_{xx} = -z \left(v'' + \frac{1}{2} v'^2 v'' \right) \quad (9)$$

where v is the transversal displacement. The notation (\cdot) is the derivative with respect to x . Making use of the Galerkin method, we use the following trial function

$$v(x, t) = \sum_{n=1}^m \varphi_n(x) r_n(t) \quad (10)$$

where n is the number of mode shapes. To simplify the derivations, the first mode shape of the cantilever beam is used ($n = 1$)

$$\varphi(x) = C_4 \left[\cosh \tilde{\lambda} x - \cos \tilde{\lambda} x - \frac{\cosh \tilde{\lambda} L + \cos \tilde{\lambda} L}{\sinh \tilde{\lambda} L + \sin \tilde{\lambda} L} (\sinh \tilde{\lambda} x - \sin \tilde{\lambda} x) \right] \quad (11)$$

where $\tilde{\lambda}$ and C_4 are determined by the following equations

$$\tilde{\lambda} L = 1.875 \quad (12)$$

$$(\rho_p A_p + \rho_s A_s + \rho_b A_b) \int_0^L \varphi^2(x) dx = 1 \quad (13)$$

Using Hamilton's principle, the dynamic equation of the system can be established.

$$\delta \int_{t_0}^{t_1} (T - U) dt + \int_{t_0}^{t_1} \delta W dt = 0 \quad (14)$$

Substituting Eqs. (3), (5) and (7) into (14) yields the governing motion of the system

$$\left\{ \begin{array}{l} \ddot{r} + 2\zeta_1 \omega_1^2 \dot{r} + \omega_1 r - \mu_2 \dot{s} - \chi_2 s - \varphi_L f(s, \dot{s}) - \theta_p V_1 - \theta_{p1} r^2 V_1 + \kappa \dot{z} + \kappa_1 r^3 + \kappa_2 r^5 + \theta_{p2} V_2 = 0 \\ C_{p1} \dot{V}_1 + \frac{V_1}{R_{L1}} + \theta_p \dot{r} + \theta_{p1} r^2 \dot{r} = 0 \\ \ddot{s} + 2\zeta_2 \omega_2 \dot{s} + \omega_2^2 s + \frac{1}{m} f(s, \dot{s}) - \frac{\theta_2}{m} V_2 + \varphi_L \ddot{r} + \ddot{z} = 0 \\ C_{p2} \dot{V}_2 + \frac{V_2}{R_{L2}} + \theta_2 \dot{s} = 0 \end{array} \right. , \quad (15)$$

here $V_1 = \dot{\lambda}_1$, $V_2 = \dot{\lambda}_2$. R_{L1} and R_{L2} are the resistance of the overlapped part and the upper separate layer, respectively. The other parameters are listed in Appendix A.

By introducing the dimensionless transformations $\tau = \omega_1 t$, $x_1 = r/L$, $x_2 = s/L$, $v_1 = C_{p1} V_1 / \theta_p L$ and $v_2 = C_{p2} V_2 / \theta_2 L$, then Eq. (15) can be expressed in a dimensionless and simplified form as follows:

$$\begin{cases} \dot{x}_1 + 2\zeta_1\dot{x}_1 + x_1 - a_1\dot{x}_2 - a_2x_2 - b_1f_0(x_2, \dot{x}_2) - \theta_1v_1 - \theta_2x_1^2v_1 + \theta_e v_2 + a_3x_1^3 - a_4x_1^5 + p_1\cos(\Omega\tau) = 0 \\ \dot{v}_1 + \xi_1v_1 + \dot{x}_1 + \gamma_1x_1^2\dot{x}_1 = 0 \\ \dot{x}_2 + 2\zeta_2v\dot{x}_2 + v^2x_2 + b_2f_0(x_2, \dot{x}_2) - \theta_3v_2 + \mu\dot{x}_1 + p_2\cos(\Omega\tau) = 0 \\ \dot{v}_2 + \xi_2v_2 + \dot{x}_2 = 0 \end{cases} \quad (16)$$

where the parameters see Appendix B for details.

3.2 Approximate analytical solutions

The averaging method is a common approach for solving nonlinear dynamic equations (Liu et al., 2016; Zhao et al., 2018a). To study the impact effect on the system, the second, third and fifth terms of Eq. (16) are neglected. We assume $X_1 = x_2$, $X_2 = \dot{x}_2$, $X_3 = x_1$, $X_4 = \dot{x}_1$, $X_5 = v_2$, $X_6 = v_1$ and introduce the parameters F_2 and F_4 . Therefore, Eq. (16) can be expressed as follows:

$$\begin{cases} \dot{X}_1 = X_2 \\ \dot{X}_2 = -\hat{a}_2X_1 + \mu X_3 + F_2 \\ \dot{X}_3 = X_4 \\ \dot{X}_4 = a_2X_1 - X_3 + F_4 \\ \dot{X}_5 = -X_2 - \xi_2X_5 \\ \dot{X}_6 = -X_4 - \xi_1X_6 \end{cases} \quad (17)$$

where

$$\begin{aligned} \hat{a}_2 &= v^2 + \mu a_2 \\ F_2 &= -(p_2 - \mu p_1)\cos(\Omega\tau) + 2\mu\zeta_1X_4 - (2\zeta_2v + \mu a_1)X_2 - (\mu b_1 + b_2)f_0(X_1, X_2) \\ &\quad - \mu\theta_1X_6 + (\mu\theta_e + \theta_3)X_5 \\ F_4 &= -p_1\cos(\Omega\tau) - 2\zeta_1X_4 + a_1X_2 + b_1f_0(X_1, X_2) + \theta_1X_6 - \theta_eX_5 \end{aligned} \quad (18)$$

Let $F_2 = F_4 = 0$, we get the following equation in a matrix form

$$\dot{X} = AX \quad (19)$$

where A is a coefficient matrix. The solutions of the derived linear equations can be expressed as $X_j = C_j e^{i\lambda\tau}$ ($j = 1, 2, \dots, 6$), and the first and second natural frequencies of the derived linear equations can be obtained by substituting the solutions into Eq. (19).

$$\lambda_{1,2}^2 = \frac{1}{2}(\hat{a}_2 + 1) \mp \frac{1}{2}\sqrt{(\hat{a}_2 + 1)^2 - 4v^2} \quad (20)$$

The fundamental solutions of the derived linear equations φ_{sk} and the form of φ_{sk}^* can be obtained easily. When $C_1 = 1$, φ_{sk} and φ_{sk}^* are the real and imaginary parts of $X_j = C_j e^{i\lambda\tau}$. And here, the φ_{sk} and φ_{sk}^* are expressed in Appendix C for detail.

The conjugate equations of the derived linear equations can be obtained as

$$\dot{Y} = -A^T Y \quad (21)$$

And the fundamental solutions of the conjugate equations $\psi_{sj}(\theta_j)$ and the forms of $\psi_{sj}^*(\theta_j)$ can see Appendix D for detail.

The orthogonal relationships between $\varphi_{si}(\theta_i)$, $\varphi_{si}^*(\theta_i)$ and $\psi_{sj}(\theta_j)$, $\psi_{sj}^*(\theta_j)$ can be proved easily.

$$\sum_{s=1}^6 \varphi_{si}(\theta_i)\psi_{sj}(\theta_j) = \sum_{s=1}^6 \varphi_{si}(\theta_i)\psi_{sj}^*(\theta_j) = 0, (i \neq j) \quad (22a)$$

$$\sum_{s=1}^6 \varphi_{si}^*(\theta_i)\psi_{sj}(\theta_j) = \sum_{s=1}^6 \varphi_{si}^*(\theta_i)\psi_{sj}^*(\theta_j) = 0, (i \neq j) \quad (22b)$$

$$\sum_{s=1}^6 \varphi_{si}(\theta_i)\psi_{sj}^*(\theta_j) = \sum_{s=1}^6 \varphi_{si}^*(\theta_i)\psi_{sj}(\theta_j) = 0, (i \neq j) \quad (22c)$$

$$\sum_{s=1}^6 \varphi_{si}(\theta_i)\psi_{sj}(\theta_j) = \sum_{s=1}^6 \varphi_{si}^*(\theta_i)\psi_{sj}^*(\theta_j) = 1 + \frac{1}{\mu a_2}(\hat{a}_2 - \lambda_i^2)^2 = \Delta_i, (i \neq j) \quad (22d)$$

When the averaging method is used to analyze the nonlinear system, the approximate solutions of Eq. (17) can be assumed as

$$X_s = \sum_{k=1}^2 B_k \varphi_{sk}(\theta_k) \quad (s = 1, 2, 3, 4, 5, 6) \quad (23)$$

where the parameters B_k and θ_k are amplitude and phase angle, which are functions of τ . The phase angle can be expressed as $\theta_k = \Omega\tau + \vartheta_k$, where ϑ_k is the initial phase angle.

When $d\theta_k/d\tau = \lambda_k$, $\varphi_{sk}(\theta_k)$ and λ_k are the special solution and natural frequency of the derived linear equations. When B_k is a constant and $d\theta_k/d\tau = \lambda_k$, Eq. (23) is the general solution of the derived equation system. The following expression is obtained by substituting Eq. (23) into Eq. (17)

$$\sum_{k=1}^2 \frac{dB_k}{d\tau} \varphi_{sk}(\theta_k) - \sum_{k=1}^2 B_k \varphi_{sk}^*(\theta_k) \left(\frac{d\theta_k}{d\tau} - \lambda_k \right) = \bar{F}_s \quad (s = 1, 2, \dots, 6) \quad (24)$$

Where $\bar{F}_1 = \bar{F}_3 = \bar{F}_5 = \bar{F}_6 = 0$, $\bar{F}_2 = F_2$, $\bar{F}_4 = F_4$.

Due to the orthogonal relationships in Eq. (22), the expressions $dB_k/d\tau$ and $d\theta_k/d\tau$ can be obtained by multiplying $\psi_{si}(\theta_i)$ and $\psi_{si}^*(\theta_i)$ with Eq. (30) separately, we have

$$\begin{aligned} \frac{dB_k}{d\tau} &= \frac{1}{\Delta_k} \sum_{s=1}^6 \bar{F}_s \psi_{sk}(\theta_k) = \phi_k(B, \theta) \\ \frac{d\theta_k}{d\tau} &= \lambda_k - \frac{1}{\Delta_k B_k} \sum_{s=1}^6 \bar{F}_s \psi_{sk}^*(\theta_k) = \lambda_k - \phi_k^*(B, \theta) \end{aligned} \quad (25)$$

In the case of resonance, $\lambda_k - \Omega$ is approximately equal to zero, and $d\vartheta_k/d\tau = d\theta_k/d\tau - \Omega$. Compared with the linear terms, \bar{F}_s is a negligible term. From Eq. (25), B_k and θ_k are functions of slowly varying relative time. Hence, $dB_k/d\tau$ and $d\vartheta_k/d\tau$ can be obtained as follows:

$$\begin{aligned} \frac{dB_k}{d\tau} &= \frac{1}{T} \int_0^T \phi_k d\tau = \frac{1}{2\pi} \int_0^{2\pi} \phi_k d\theta_k \\ \frac{d\vartheta_k}{d\tau} &= \frac{1}{T} \int_0^T (\lambda_k - \Omega - \phi_k^*) d\tau = \lambda_k - \Omega - \frac{1}{2\pi} \int_0^{2\pi} \phi_k^* d\theta_k \end{aligned} \quad (26)$$

When the system is working under one of the resonant regions, the amplitude in other resonant regions has little impact on the displacement of the system. Therefore, taking the

second-order resonant region into consideration, B_1 is assumed to be zero. The approximate solutions (23) can be approximated to $X_s = B_2\varphi_{s2}(\theta_2)$. So, ϕ_2 and ϕ_2^* in Eq. (25) can be calculated as follows:

$$\begin{aligned}\phi_2 &= \frac{1}{\Delta_2} \sum_{s=1}^6 \bar{F}_s \psi_{s2}(\theta_2) \\ &= \frac{1}{\Delta_2} \left\{ \begin{aligned} &-(p_2 - \mu p_1) \cos(\Omega\tau) - 2\mu\zeta_1 B_2 \frac{\lambda_2(\hat{a}_2 - \lambda_2^2)}{\mu} \sin\theta_2 + (2\zeta_2 v + \mu a_1) B_2 \lambda_2 \sin\theta_2 \\ &-(\mu b_1 + b_2) f_0(B_2, \theta_2) - \mu\theta_1 \frac{B_2 \lambda_2(\hat{a}_2 - \lambda_2^2)}{\mu(\xi_2^2 + \lambda_2^2)} (\xi_1 \sin\theta_2 - \lambda_2 \cos\theta_2) \\ &+ (\mu\theta_e + \theta_3) \frac{B_2 \lambda_2}{\xi_2^2 + \lambda_2^2} (\xi_2 \sin\theta_2 - \lambda_2 \cos\theta_2) \end{aligned} \right\} \left(-\frac{1}{\lambda_2} \sin\theta_2 \right) \\ &+ \frac{1}{\Delta_2} \left\{ \begin{aligned} &-p_1 \cos(\Omega\tau) + 2\zeta_1 B_2 \frac{\lambda_2(\hat{a}_2 - \lambda_2^2)}{\mu} \sin\theta_2 - a_1 B_2 \lambda_2 \sin\theta_2 + b_1 f_0(B_2, \theta_2) \\ &+ \theta_1 \frac{B_2 \lambda_2(\hat{a}_2 - \lambda_2^2)}{\mu(\xi_1^2 + \lambda_2^2)} (\xi_1 \sin\theta_2 - \lambda_2 \cos\theta_2) - \theta_e \frac{B_2 \lambda_2}{\xi_2^2 + \lambda_2^2} (\xi_2 \sin\theta_2 - \lambda_2 \cos\theta_2) \end{aligned} \right\} \left(-\frac{\hat{a}_2 - \lambda_2^2}{a_2 \lambda_2} \sin\theta_2 \right) \end{aligned} \quad (27a)$$

$$\begin{aligned}\phi_2^* &= \frac{1}{\Delta_2 B_2} \sum_{s=1}^6 \bar{F}_s \psi_{s2}^*(\theta_2) \\ &= \frac{1}{\Delta_2 B_2} \left\{ \begin{aligned} &-(p_2 - \mu p_1) \cos(\Omega\tau) - 2\mu\zeta_1 B_2 \frac{\lambda_2(\hat{a}_2 - \lambda_2^2)}{\mu} \sin\theta_2 + (2\zeta_2 v + \mu a_1) B_2 \lambda_2 \sin\theta_2 \\ &-(\mu b_1 + b_2) f_0(B_2, \theta_2) - \mu\theta_1 \frac{B_2 \lambda_2(\hat{a}_2 - \lambda_2^2)}{\mu(\xi_1^2 + \lambda_2^2)} (\xi_1 \sin\theta_2 - \lambda_2 \cos\theta_2) \\ &+ (\mu\theta_e + \theta_3) \frac{B_2 \lambda_2}{\xi_2^2 + \lambda_2^2} (\xi_2 \sin\theta_2 - \lambda_2 \cos\theta_2) \end{aligned} \right\} \left(\frac{1}{\lambda_2} \cos\theta_2 \right) \\ &+ \frac{1}{\Delta_2 B_2} \left\{ \begin{aligned} &-p_1 \cos(\Omega\tau) + 2\zeta_1 B_2 \frac{\lambda_2(\hat{a}_2 - \lambda_2^2)}{\mu} \sin\theta_2 - a_1 B_2 \lambda_2 \sin\theta_2 + b_1 f_0(B_2, \theta_2) \\ &+ \theta_1 \frac{B_2 \lambda_2(\hat{a}_2 - \lambda_2^2)}{\mu(\xi_1^2 + \lambda_2^2)} (\xi_1 \sin\theta_2 - \lambda_2 \cos\theta_2) - \theta_e \frac{B_2 \lambda_2}{\xi_2^2 + \lambda_2^2} (\xi_2 \sin\theta_2 - \lambda_2 \cos\theta_2) \end{aligned} \right\} \left(\frac{\hat{a}_2 - \lambda_2^2}{a_2 \lambda_2} \cos\theta_2 \right) \end{aligned} \quad (27b)$$

where $f_0(B_2, \theta_2)$ is a piecewise function, and the Fourier series expansion of its first harmonic term is

$$f_0(B_2, \theta_2) = \frac{1}{\pi} B_2 \left[\frac{2k}{\omega_1} h_1 + \left(\frac{k}{\omega_1} \cos\theta_2 - c \lambda_2 \sin\theta_2 \right) h_0 \right] \quad (28)$$

where $\theta_0 = \arccos(e/B_2)$, $h_0 = \theta_0 - \sin\theta_0 \cos\theta_0$, $h_1 = (\theta_0 \cos\theta_0 - \sin\theta_0)$.

Finally, the expressions of $dB_2/d\tau$ and $d\vartheta_2/d\tau$ can be obtained

$$\begin{aligned}\frac{dB_2}{d\tau} &= \frac{1}{2\Delta_2 \lambda_2} \left(p_2 - \mu p_1 + p_1 \frac{\hat{a}_2 - \lambda_2^2}{a_2} \right) \sin\vartheta_2 - B_2 \eta_e(B_2) \\ \frac{d\vartheta_2}{d\tau} &= \frac{1}{2\Delta_2 B_2 \lambda_2} \left(p_2 - \mu p_1 + p_1 \frac{\hat{a}_2 - \lambda_2^2}{a_2} \right) \cos\vartheta_2 + \omega_e(B_2) - \Omega \end{aligned} \quad (29)$$

where $\omega_e(B_2)$ and $\eta_e(B_2)$ are the equivalent natural frequency and equivalent attenuation coefficient, respectively. They are

$$\begin{aligned}\omega_e(B_2) &= \lambda_2 + \frac{1}{2\Delta_2} \left\{ \left(\mu b_1 + b_2 - b_1 \frac{\hat{a}_2 - \lambda_2^2}{a_2} \right) \frac{k h_0}{\pi \omega_1 \lambda_2} + \left(\theta_1 \frac{\hat{a}_2 - \lambda_2^2}{a_2} - \mu\theta_1 \right) \frac{\lambda_2(\hat{a}_2 - \lambda_2^2)}{\mu(\xi_2^2 + \lambda_2^2)} \right. \\ &\quad \left. + \left(\mu\theta_e + \theta_3 - \theta_e \frac{\hat{a}_2 - \lambda_2^2}{a_2} \right) \frac{\lambda_2}{\xi_2^2 + \lambda_2^2} \right\} \end{aligned} \quad (30a)$$

$$\begin{aligned} \eta_e(B_2) = & \frac{1}{2\Delta_2} \left\{ \left(\mu b_1 + b_2 - b_1 \frac{\hat{a}_2 - \lambda_2^2}{a_2} \right) \frac{ch_0}{\pi} + \left(\Theta_1 \frac{\hat{a}_2 - \lambda_2^2}{a_2} - \mu \Theta_1 \right) \frac{\xi_1(\hat{a}_2 - \lambda_2^2)}{\mu(\xi_1^2 + \lambda_2^2)} \right. \\ & + \left(\mu \Theta_e + \Theta_3 - \Theta_e \frac{\hat{a}_2 - \lambda_2^2}{a_2} \right) \frac{\xi_2}{\xi_2^2 + \lambda_2^2} \\ & \left. + \left[2\zeta_2 v + \mu a_1 + \frac{2\zeta_1}{\mu a_2} (\hat{a}_2 - \lambda_2^2)^2 - \left(2\zeta_1 + \frac{a_1}{a_2} \right) (\hat{a}_2 - \lambda_2^2) \right] \right\} \end{aligned} \quad (30b)$$

As discussed above, the variations of B_2 and ϑ_2 are slowly changed. Hence, the terms $dB_2/d\tau$ and $d\vartheta_2/d\tau$ can be assumed as zero. The following expressions are obtained

$$\frac{1}{\Delta_2} \left[(p_2 - \mu p_1) + p_1 \frac{\hat{a}_2 - \lambda_2^2}{a_2} \right] \sin \vartheta_2 = 2\lambda_2 B_2 \eta_e(B_2) \quad (31a)$$

$$-\frac{1}{\Delta_2} \left[(p_2 - \mu p_1) + p_1 \frac{\hat{a}_2 - \lambda_2^2}{a_2} \right] \cos \vartheta_2 = 2\lambda_2 B_2 (\omega_e(B_2) - \Omega) \quad (31b)$$

Since the system vibrates in the second resonant region, the parameter $2\lambda_2$ in Eq. (31) can be approximately replaced by 2Ω and $\omega_e(B_2) + \Omega$, respectively. Then, the expression of the amplitude-frequency response of amplitude B relative to the excitation frequency can be derived as follows:

$$B_2 = \frac{(p_2 - \mu p_1) + p_1 \frac{\hat{a}_2 - \lambda_2^2}{a_2}}{\Delta_2 \sqrt{(\omega_e^2(B_2) - \Omega^2)^2 + 4\Omega^2 \eta_e^2(B_2)}} \quad (32)$$

By replacing the parameters B_2 , ϑ_2 , λ_2 and Δ_2 with the parameters B_1 , ϑ_1 , λ_1 and Δ_1 , the relationship between the amplitude B_1 and the external excitation frequency Ω can be obtained.

Setting $X_5 = v_2$ and $X_6 = v_1$, the total output voltage of the system is given by

$$v_k = v_{1k} + v_{2k} = B_k \frac{\lambda_k(\hat{a}_2 - \lambda_k^2)}{\mu \sqrt{\xi_2^2 + \lambda_k^2}} + B_k \frac{\lambda_k}{\sqrt{\xi_2^2 + \lambda_k^2}} \quad (33)$$

3.3 Numerical results and discussion

3.3.1 Analysis of energy harvesting characteristics

The material properties and the structural parameters of piezoelectric cantilever beams are shown in Table 1. To measure the open circuit voltage of the system, the load resistances R_{L1} and R_{L2} are set to 20 M Ω , which are much larger than the internal resistances of the upper separated layer and the overlapped part, respectively. The gap distance is set to 0.3 mm. Subject to an external excitation of 0.2g, both the thickness of the piezoelectric and fundamental layers is 0.3 mm, and the tip mass is 0.6g. Results of the open circuit voltage under a frequency range of 0-100 Hz is presented in Fig. 2. It is seen that the open circuit voltage (V_k) of the system has two nonlinear peak value. The results can be divided into five stages to explain the impact mechanism clearly.

Table 1 Material parameters of the piezoelectric energy harvester

Parameter	Value
Beam	
Length of overlapped part L	50 mm
Length of separated part L_2	25 mm
Width b	10 mm
Tip mass m_t	0.0006 kg
Piezoelectric layer	
Young's modulus C_{xx}^E	2.5 GPa
Piezoelectric strain coefficient d_{zx}	-18 pC/N
Laminate permittivity ϵ_{zz}^S	2.18 nF/m
Thickness h_p	0.3 mm
Density ρ_p	2000 kg/m ³
Protective layer	
Young's modulus E_s	3 GPa
Thickness h_s	0.1 mm
Density ρ_s	1000 kg/m ³
Fundamental layer	
Young's modulus E_b	90 GPa
Thickness h_b	0.3 mm
Density ρ_b	8900 kg/m ³
Lumped mass part	
Capacitance of separate piezoelectric layer C_{p2}	1.82 nF
Stiffness of the upper separate layer k_2	27.7 N/m
Damping of the upper separate layer c_2	0.002 kgs ⁻¹
Stiffness of the lower separate layer k	129.6 N/m
Damping of the lower separate layer c	0.005 kgs ⁻¹
Gap distance d	0.3 mm

Stage I starts from point A to point B, where the open circuit voltage is mainly determined by the amplitude of the upper separated layer in the first resonant region. It grows gradually with frequency. Stage II is from point B to point C, where the end of the upper separated layer with the tip mass reaches the gap distance d and makes collision with the lower separated layer. During the impact, the stiffness and damping of the upper separated layer can be increased due to the lower separated layer (as a stopper). As a result, the first equivalent natural frequency is enlarged, thereby broadening the frequency bandwidth of the vibro-impact harvester. Stage III starts at point C, where the hard spring characteristic occurs and the open circuit voltage of the system drops dramatically to point D. The open circuit voltage decreases sharply until the frequency is at the second resonant region. Stages IV and V in the second resonant region repeat the same process of the previous one in the first resonant region.

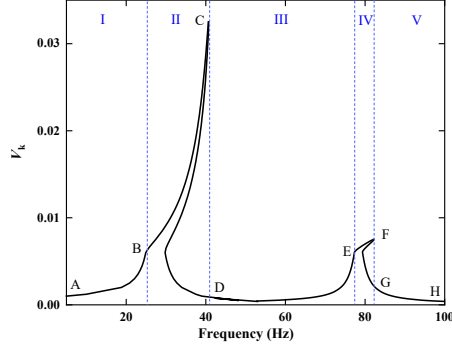


Fig. 2 Open circuit voltage versus frequency of the proposed harvester

3.3.2 Influence of parameters

Effects of various parameters, such as the thickness of the piezoelectric layer (h_p), the thickness of the fundamental layer (h_b), the tip mass (m_t) at the end of the upper separated layer and the external excitation acceleration (A), on the system are investigated in this work.

When $A = 0.2g$, $h_b = 0.3mm$, and $m_t = 0.6g$, the open circuit voltage under different values of h_p is shown in Fig. 3. It is seen that the open circuit voltage curve of the proposed harvester deviates to the right side when the voltage reaches a critical value. A smaller value of h_p can result in a larger deflection. This is because a comparatively small h_p will reduce the first natural frequency of the harvester and the stiffness ratio of the upper and lower separated layers, resulting in an increase of equivalent natural frequency. Hence, more nonlinearity will be introduced to the system, as shown in Eq. (37). The peak voltage increases gradually while the frequency bandwidth decreases with the increases of h_p in the first resonant region, and the peak voltage and frequency bandwidth in the second resonant region decrease accordingly.

Setting $A = 0.2g$, $h_p=0.3mm$ and $m_t = 0.6g$, the open circuit voltage under various values of h_b is presented in Fig. 4. To increase the value of h_b , the peak voltage decreases as the frequency bandwidth becomes wider in the first resonant region. Both the peak voltage and the frequency bandwidth increase accordingly in the second resonant region. The reason is that a comparatively large h_b will increase the first natural frequency of the harvester and decrease the stiffness ratio of the upper and lower separated layers. Therefore, nonlinearity will be introduced to the system. When $h_b=0.2 mm$, the relative displacement of the separated parts in the second resonant region is less than the gap distance, there is no nonlinear effect in the second resonant region.

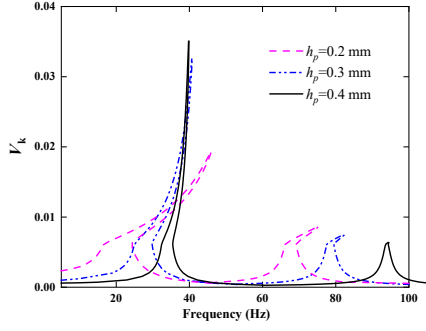


Fig. 3 Open circuit voltage versus frequency under different thickness of the piezoelectric layer

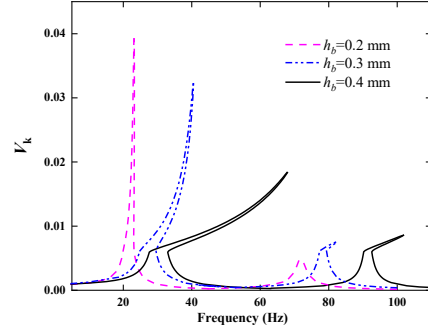


Fig. 4 Open circuit voltage versus frequency under different thickness of the fundamental layer

In another case ($A = 0.2g$ and $h_b = h_p = 0.3mm$, the open circuit voltage under different values of m_t is plotted in Fig. 5. In the first resonant region, the peak voltage increases gradually to a peak value and then decreases as the frequency bandwidth increases. However, the voltage decreases with the reduction of m_t . In the second resonant region, the responses are similar to those responses in the first resonant region, but the voltage levels are much smaller. In addition, the frequency range between the first and second resonant regions increases. Because the parameter m_t can change the stiffness of the upper separated layer, this would affect the first natural frequency.

When we further consider $m_t = 0.6g$ and $h_b = h_p = 0.3mm$, the open circuit voltage under different values of A is shown in Fig. 6. The change of the amplitude-frequency response curves is the same in the first resonant region, but they are of different critical voltage levels. A larger value of A can enlarge the frequency of peak voltage. This is because it will induce more energy acting on the harvester, resulting in a larger output voltage under the same frequency. In addition, the output voltage in the second resonant region shows a linear effect for $A = 0.1g$. It implies that the upper separated layer can hardly hit the lower separated layer in this region when A is smaller than $0.1g$.

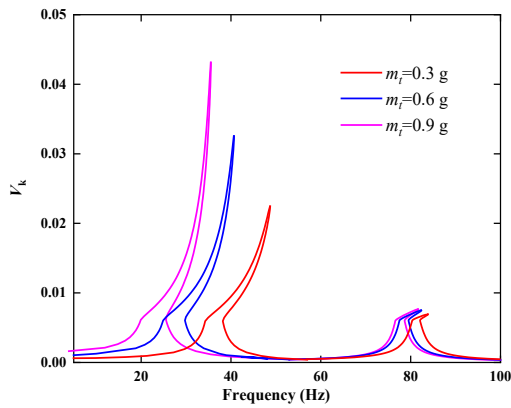


Fig. 5 Open circuit voltage versus frequency under different tip mass

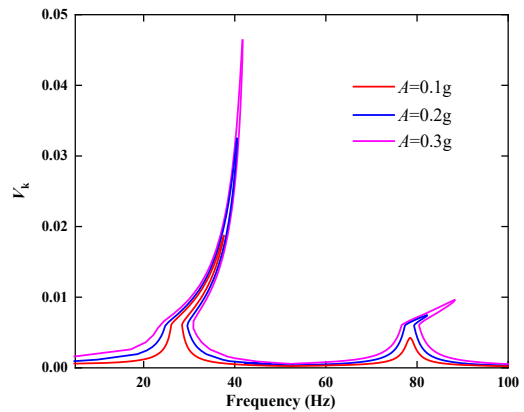


Fig. 6 Open circuit voltage versus frequency under different acceleration

4. Experimental validation

4.1 Materials and geometric dimensions

Piezoelectric materials used in the experiment are PVDF, this type of material possesses good flexibility, low density and high stability. In the experiment, the partially separated parts of the piezoelectric beam would collide with each other during cyclic motions, the flexibility of PVDF can make it more persistent during impact. The piezoelectric beam used in the experiment is shown in Figs. 7(a) and (b). The protective layer and the fundamental layer were bonded on the two surfaces of the polarized piezoelectric layer. The protective layer was made of polyester while the fundamental layer was made of brass. In addition to the separated parts, the layers were well bonded by an electric glue. There is no relative slip between the layers when the bending deformation of the beam occurs during vibration. However, there is a small gap distance between the upper and lower separated layers due to their residual stress. In the experiment, the gap distance was maintained at 0.3 mm. Two conducting wires were induced from the upper surface of the piezoelectric layer and the lower surface of the base layer, respectively. The effective length and width of the piezoelectric beam were 75 mm and 10 mm, respectively. The separated length of the beam was 25 mm. The thickness of the piezoelectric, protective and fundamental layers was 0.3 mm, 0.3 mm and 0.1 mm, respectively. The material parameters of the piezoelectric beam are listed in Table 1. Auxiliary materials used in the experiment are shown in Fig. 7(c), e.g., conducting wires, ruler, proof mass and resistors etc. A fabricated prototype of the proposed piezoelectric energy harvester is presented in Fig. 7(d).

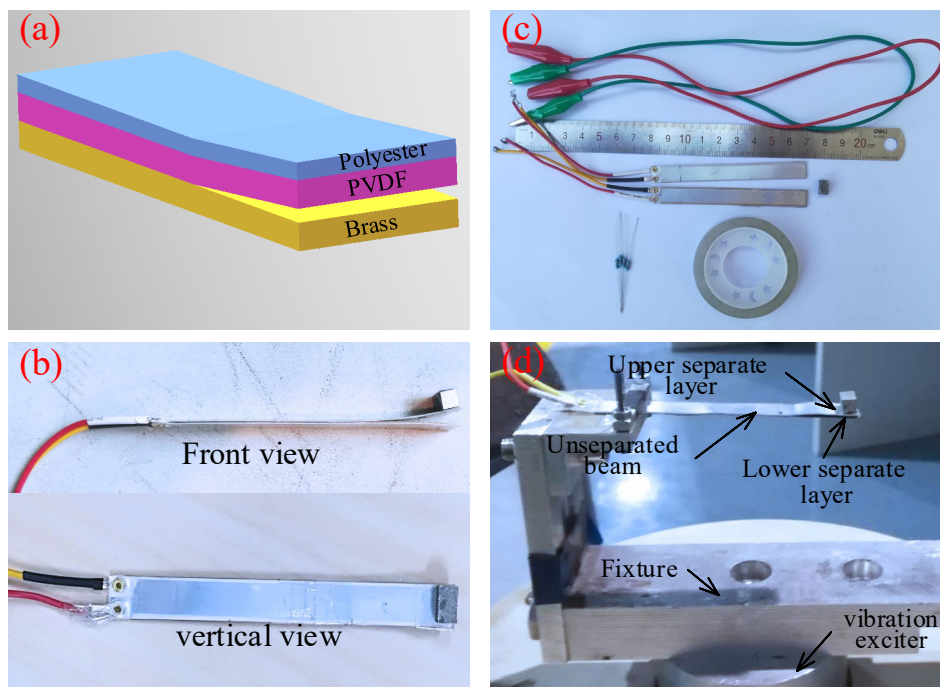


Fig. 7 Experimental materials and prototype: (a) a three-dimensional model of the proposed piezoelectric beam; (b) a fabricated model of piezoelectric beam; (c) auxiliary materials; and (d) a

fabricated prototype of the proposed piezoelectric energy harvester

4.2 Experimental results

Fig. 8 demonstrates the experimental setup, which includes a signal generator, a power amplifier, a JZK series exciter, a laser displacement sensor, a controller, a digital oscilloscope and a multi-meter. In addition, a software used in the experiment was a LK-Navigator. To ignore the influence of geometric nonlinearity, the deflection of the piezoelectric beam under different excitation accelerations was measured by the laser displacement sensor to ensure that the movement of the beam was not a large deformation. The excitation frequency was increased gradually from 5 Hz to 80 Hz by adjusting the signal generator manually. The output voltage values were displayed and recorded by a digital oscilloscope directly.

The experiment results under the acceleration of 0.2g are presented in Fig. 9, where the red curve and blue curve correspond to the open circuit voltage results of the proposed harvester and a traditional harvester, respectively. Here, the traditional harvester means the piezoelectric cantilever beam has no any interlayer-separated feature. That is to say, the structure of the traditional harvester is same as the proposed harvester, which consists of a protective layer, a piezoelectric layer and a fundamental layer. The material, the length, the thickness and the width of each layer are also same as those of the proposed harvester. The peak voltage of the traditional harvester is 0.52 V, while two peak voltages of the proposed harvester are 1.92 V and 0.71 V, respectively. It is found that the peak voltage and frequency bandwidth of the proposed harvester are better than those of the traditional harvester. When the output voltage reaches the peak values in the first and second resonant regions, the external excitation frequencies are at 26 Hz and 56 Hz, respectively.



Fig. 8 The experimental equipment

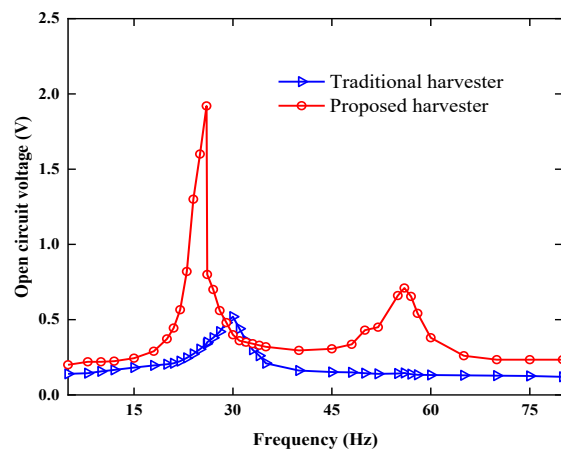


Fig. 9 Open circuit voltage of the proposed harvester and a traditional harvester

The output powers of the proposed and traditional harvesters under various load resistance at 26 Hz and 30 Hz are shown in Fig. 10. For these two kinds of harvesters, the

output power increases first and then decreases when increasing the load resistance. The maximum power of $0.605 \mu\text{W}$ and $0.048 \mu\text{W}$ can be obtained under their optimal load resistance values at $1.5 \text{ M}\Omega$ and $1.3 \text{ M}\Omega$, respectively. The maximum power of the proposed harvester is 12.6 times than that of the traditional harvester.

Under the optimal load resistance levels, the output power of the proposed harvester and the traditional harvester is given in Fig. 11. It is seen that the changing trend of the amplitude-frequency response curves are similar to that of the open circuit voltage. The output power of the proposed harvester is larger than that of the traditional harvester in the frequency range from 5 Hz to 29 Hz and 32 Hz to 80 Hz. When the frequency varies from 29 Hz to 32 Hz, the output power of the traditional harvester is slightly greater than that of the proposed harvester. Consider the overall output power and frequency bandwidth, the power generation performance of the proposed harvester is much better than that of the traditional harvester.

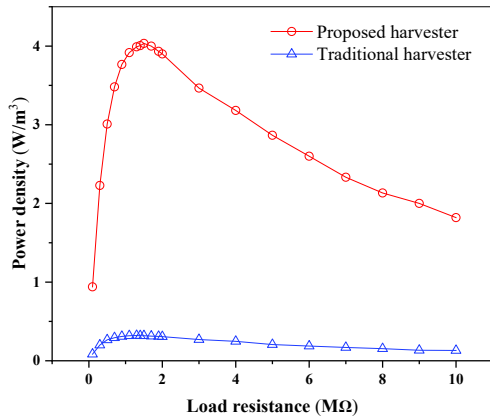


Fig. 10 Output power density of the proposed and traditional harvesters under 26Hz and 30Hz, respectively

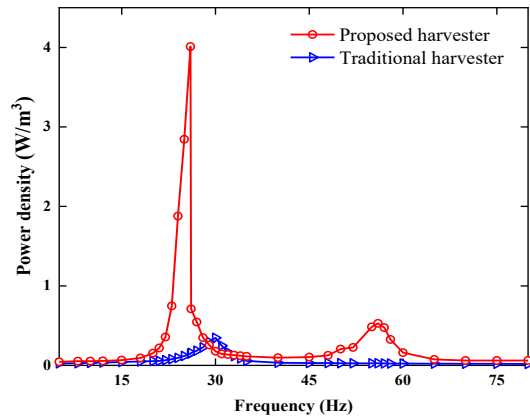


Fig. 11 Output power density of the proposed and traditional harvesters under $1.5 \text{ M}\Omega$ and $1.3 \text{ M}\Omega$, respectively

When the acceleration is 0.2g , the open circuit voltage of the proposed harvester under different tip masses is shown in Fig. 12. The output voltage of the system under different tip masses has two peaks. The first peak voltage is larger while the second peak voltage is smaller. When the tip masses are 0.3g , 0.6g and 0.9g , the system achieves the first peak voltage at 1.72 V , 1.92 V and 2.2 V at 31 Hz , 26 Hz and 23 Hz , respectively. Under the same acceleration conditions, the second peak voltage of 0.56 V , 0.7 V and 0.44 V can be achieved at 61.5 Hz , 56 Hz and 62 Hz , respectively. The results demonstrate that the peak voltage increases while the frequency bandwidth increases first and then decreases in the first resonant region by increasing the tip mass. The peak voltage and frequency bandwidth in the second resonant region increase first and then decrease accordingly. In addition, the frequency at the first peak voltage decreases gradually with the increase of the tip mass, and the changing trends of the open circuit voltage of the experimental results agree well with

that of the theoretical results.

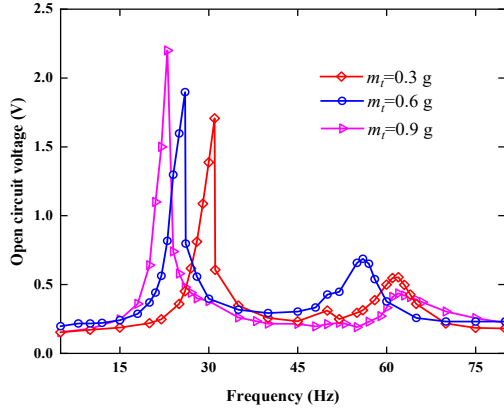


Fig. 12 Open circuit voltage of the harvester under different tip masses

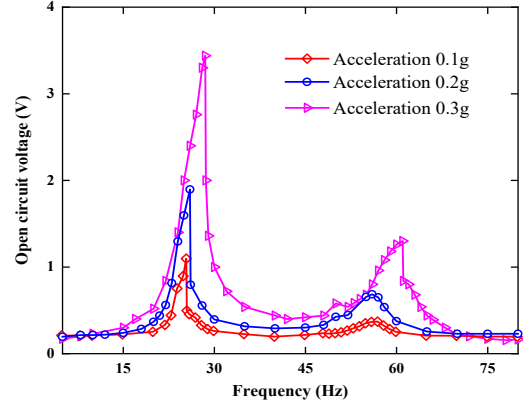


Fig. 13 Open circuit voltage of the harvester under different accelerations

When the tip mass is increased to 0.6g, the open circuit voltage of the proposed harvester under different accelerations is given in Fig. 13. Under the acceleration levels of 0.1 - 0.3 g, the system can achieve the first peak voltage of 1.1 V, 1.92 V and 3.44 V at 25.5 Hz, 26 Hz and 28.5 Hz, and the second peak voltage of 0.37 V, 0.7 V and 1.3 V at 57 Hz, 56 Hz and 61 Hz, respectively. By increasing the acceleration, the frequency at the peak voltage increases gradually, the waveforms are quite similar to the theoretical results, where the peak voltage and frequency bandwidth increase as the acceleration increases. In addition, the output voltage in the second resonant region does not show a nonlinear effect at the acceleration of 0.1g, because the upper separated layer can hardly hit the lower separated layer under this condition. This is consistent with the finding of the theoretical analysis.

5. Conclusions

In this study, a vibro-impact piezoelectric vibration energy harvester based on a partial interlayer-separated piezoelectric beam is proposed to enhance the output power and frequency bandwidth of the system. The electromechanical coupling equation is derived, and approximate analytical solutions are constructed by using the averaging method. Numerical simulations and experimental results show that two voltage peaks are found both in the first and second resonant regions. The peak voltage and frequency bandwidth of the proposed harvester are larger than those of the traditional harvester. The maximum power of 0.605 μW of the proposed harvester in the first resonant region, which is 12.6 times than that of the traditional harvester of 0.048 μW under the acceleration of 0.2g. Optimizing the structure parameters of the harvester can achieve a better power generation performance. For example, to increase the thickness of the piezoelectric layer h_p and the tip mass m_t , and decrease the thickness of the fundamental layer h_b will increase the first voltage peak of the harvester. Moreover, the change of the parameters h_p and h_b will lead to a wider

frequency bandwidth, and shift the frequency at the peak voltage.

Comparing with the previous research work (Cao et al., 2019c), it is found that the first and second resonant frequencies of the partial separated VEH are smaller than that of the complete separated VEH. The results show the advantages of lower frequency and broad bandwidth energy harvesting. Although there are some errors between the theoretical and experimental results, but the shape and changing trend of the output-frequency curve from the analytical results agree well with the experimental results. Moreover, comparing with those vibro-impact energy harvester where the impact occurs between the beam and another rigid stopper (Liu et al., 2016; Zhao et al., 2018a; Hu et al., 2018), there are similar vibration responses, which means the presented theoretical and experimental models are accurate and can be used for a further optimization of the vibration energy harvester.

Conflicts of interest

The authors declare that there is no conflict of interest regarding the publication of this paper.

Acknowledgments

The authors gratefully acknowledge the support of the National Natural Science Foundation of China (Grant Nos.11672008, 11972051). The author S.K. Lai also gratefully acknowledges the financial support provided from the Early Career Scheme of the Hong Kong Research Grants Council (Project No. PolyU 252026/16E).

Appendix A

$$f(s, \dot{s}) = \begin{cases} 0 & s \geq d \\ c\dot{s} + k(s + d) & s < d \end{cases}$$

$$EI = b \int_{h_n - h_p}^{h_n} E_b z^2 dz + b \int_{h_n}^{h_n + h_p} C_{xx}^E z^2 dz + b \int_{h_n + h_p}^{h_n + h_p + h_s} E_s z^2 dz,$$

$$EI = b \int_{h_n - h_p}^{h_n} E_b z^2 dz + b \int_{h_n}^{h_n + h_p} C_{xx}^E z^2 dz + b \int_{h_n + h_p}^{h_n + h_p + h_s} E_s z^2 dz,$$

$$\omega_1^2 = EI \int_0^L \varphi''^2 dx, \quad \omega_1^2 = \frac{k_2}{m}, \quad \kappa_1 = 2EI \int_0^L \varphi' \varphi''^2 dx, \quad \kappa_2 = \frac{3}{4} EI \int_0^L \varphi'^2 \varphi''^2 dx,$$

$$\kappa = (\rho_b A_b + \rho_p A_p + \rho_s A_s) \int_0^L \varphi dx, \quad \theta_p = \frac{1}{2} (2h_n + h_p) b d_{zx} \int_0^L \varphi'' dx,$$

$$\theta_{p1} = \frac{3}{4} (2h_n + h_p) b d_{zx} \int_0^L \varphi' \varphi'' dx, \quad \zeta_1 = \frac{c_0}{2\omega_1} \int_0^L \varphi^2 dx, \quad \zeta_2 = \frac{c_2}{2m\omega_2},$$

$$C_{p1} = \frac{bL\varepsilon_{zz}^s}{h_p}, \quad \varphi_L = \varphi(L), \quad \ddot{z} = A \cos(\omega t), \quad \theta_{p2} = \varphi_L \theta_2, \quad \mu_2 = \varphi_L c_2, \quad \chi_2 = \varphi_L k_2.$$

Appendix B

$$f_0(x_2, \dot{x}_2) = \begin{cases} 0 & (x_2 \geq -e) \\ c\dot{x}_2 + \frac{k}{\omega_1}(x_2 + e) & (x_2 < -e) \end{cases}, \quad \xi_1 = \frac{1}{\omega_1 R_{L1} C_{p1}}, \quad \xi_2 = \frac{1}{\omega_1 R_{L2} C_{p2}},$$

$$\theta_1 = \frac{\theta_p^2}{c_{p1} \omega_1^2}, \quad \theta_2 = \frac{L^2 \theta_p \theta_{p1}}{c_{p1} \omega_1^2}, \quad \theta_e = \frac{\theta_2 \theta_{p2}}{c_{p2} \omega_1^2}, \quad \theta_3 = \frac{\theta_2^2}{m c_{p2} \omega_1^2}, \quad a_1 = \frac{\mu_2}{\omega_1},$$

$$a_2 = \frac{\chi_2}{\omega_1^2}, \quad a_3 = \frac{L^2 \kappa_1}{\omega_1^2}, \quad a_4 = \frac{L^4 \kappa_2}{\omega_1^2}, \quad b_1 = \frac{\varphi_L}{\omega_1}, \quad b_2 = \frac{1}{m \omega_1},$$

$$p_1 = \frac{\kappa A}{L \omega_1^2}, \quad p_2 = \frac{A}{L \omega_1^2}, \quad \mu = \varphi_L, \quad \gamma_1 = \frac{L^2 \theta_{p1}}{\theta_p}, \quad \Omega = \frac{\omega}{\omega_1}, \quad e = \frac{d}{L}, \quad \nu = \frac{\omega_2}{\omega_1}.$$

Appendix C

$$\varphi_{1k} = \cos \lambda_k \tau, \quad \varphi_{1k}^* = \sin \lambda_k \tau, \quad \varphi_{2k} = -\lambda_k \sin \lambda_k \tau, \quad \varphi_{2k}^* = \lambda_k \cos \lambda_k \tau,$$

$$\varphi_{3k} = \frac{\hat{a}_2 - \lambda_k^2}{\mu} \cos \lambda_k \tau, \quad \varphi_{3k}^* = \frac{\hat{a}_2 - \lambda_k^2}{\mu} \sin \lambda_k \tau,$$

$$\varphi_{4k} = -\frac{\lambda_k (\hat{a}_2 - \lambda_k^2)}{\mu} \sin \lambda_k \tau, \quad \varphi_{4k}^* = \frac{\lambda_k (\hat{a}_2 - \lambda_k^2)}{\mu} \cos \lambda_k \tau,$$

$$\varphi_{5k} = \frac{\lambda_k}{\xi_2^2 + \lambda_k^2} (\xi_2 \sin \lambda_k \tau - \lambda_k \cos \lambda_k \tau), \quad \varphi_{5k}^* = -\frac{\lambda_k}{\xi_2^2 + \lambda_k^2} (\lambda_k \sin \lambda_k \tau + \xi_2 \cos \lambda_k \tau),$$

$$\varphi_{6k} = \frac{\lambda_k (\hat{a}_2 - \lambda_k^2)}{\mu (\xi_1^2 + \lambda_k^2)} (\xi_1 \sin \lambda_k \tau - \lambda_k \cos \lambda_k \tau),$$

$$\varphi_{6k}^* = -\frac{\lambda_k (\hat{a}_2 - \lambda_k^2)}{\mu (\xi_1^2 + \lambda_k^2)} (\lambda_k \sin \lambda_k \tau + \xi_1 \cos \lambda_k \tau).$$

Appendix D

$$\psi_{1k} = \cos \lambda_k \tau, \quad \psi_{1k}^* = \sin \lambda_k \tau, \quad \psi_{2k} = -\frac{1}{\lambda_k} \sin \lambda_k \tau, \quad \psi_{2k}^* = \frac{1}{\lambda_k} \cos \lambda_k \tau,$$

$$\psi_{3k} = \frac{\hat{a}_2 - \lambda_k^2}{a_2} \cos \lambda_k \tau, \quad \psi_{3k}^* = \frac{\hat{a}_2 - \lambda_k^2}{a_2} \sin \lambda_k \tau,$$

$$\psi_{4k} = -\frac{\hat{a}_2 - \lambda_k^2}{a_2 \lambda_k} \sin \lambda_k \tau, \quad \psi_{4k}^* = \frac{\hat{a}_2 - \lambda_k^2}{a_2 \lambda_k} \cos \lambda_k \tau,$$

$$\psi_{5k} = \psi_{5k}^* = 0, \quad \psi_{6k} = \psi_{6k}^* = 0.$$

References

- Andò B, Baglio S, Maiorca F, et al. (2013) Analysis of two dimensional, wide-band, bistable vibration energy harvester. *Sensors and Actuators A: Physical* 202: 176-182.
- Ando B, Baglio S and Trigona C. (2010) Autonomous sensors: From standard to advanced solutions. *IEEE Instrumentation & Measurement Magazine* 13: 33-37.
- Cao DX, Ding XD, Guo XY, et al. (2020a) Improved Flow-Induced Vibration Energy Harvester by Using Magnetic Force: An Experimental Study. *International Journal of Precision Engineering and Manufacturing-Green Technology*.
- Cao DX, Duan XJ, Guo XY, et al. (2020b) Design and performance enhancement of a force-amplified piezoelectric stack energy harvester under pressure fluctuations in hydraulic pipeline systems. *Sensors and Actuators A: Physical* 309: 112031.

- Cao DX, Gao YH and Hu WH. (2019a) Modeling and power performance improvement of a piezoelectric energy harvester for low-frequency vibration environments. *Acta Mechanica Sinica* 35: 894-911.
- Cao DX, Hu WH, Gao YH, et al. (2019b) Vibration and energy harvesting performance of a piezoelectric phononic crystal beam. *Smart Materials and Structures* 28: 085014(085011-085012).
- Cao DX, Leadenham S and Erturk A. (2015) Internal resonance for nonlinear vibration energy harvesting. *European Physical Journal-Special Topics* 224: 2867-2880.
- Cao DX, Xia W and Hu WH. (2019c) Low-frequency and broadband vibration energy harvester driven by mechanical impact based on layer-separated piezoelectric beam. *Applied Mathematics and Mechanics (English Edition)* 40: 1777-1790.
- Daqaq MF, Masana R, Erturk A, et al. (2014) On the Role of Nonlinearities in Vibratory Energy Harvesting: A Critical Review and Discussion. *Applied Mechanics Reviews* 66: 040801.
- Dechant E, Fedulov F, Chashin DV, et al. (2017) Low-frequency, broadband vibration energy harvester using coupled oscillators and frequency up-conversion by mechanical stoppers. *Smart Materials and Structures* 26: 065021.
- Erturk A, Hoffmann J and Inman DJ. (2009) A piezomagnetoelastic structure for broadband vibration energy harvesting. *Applied Physics Letters* 94: 254102.
- Erturk A and Inman DJ. (2011) *Piezoelectric energy harvesting*: John Wiley & Sons.
- Fan KQ, Cai ML, Wang F, et al. (2019) A string-suspended and driven rotor for efficient ultra-low frequency mechanical energy harvesting. *Energy Conversion and Management* 198: 111820.
- Fang S, Fu X and Liao W. (2019) Asymmetric plucking bistable energy harvester: Modeling and experimental validation. *Journal of Sound and Vibration* 459: 114852.
- Fang S, Wang S, Zhou S, et al. (2020) Exploiting the advantages of the centrifugal softening effect in rotational impact energy harvesting. *Applied Physics Letters* 116: 063903.
- Fu Y, Ouyang H and Davis RB. (2018) Nonlinear dynamics and triboelectric energy harvesting from a three-degree-of-freedom vibro-impact oscillator. *Nonlinear Dynamics* 92: 1985-2004.
- Fu Y, Ouyang H and Davis RB. (2019) Triboelectric energy harvesting from the vibro-impact of three cantilevered beams. *Mechanical Systems and Signal Processing* 121: 509-531.
- Gu L. (2011) Low-frequency piezoelectric energy harvesting prototype suitable for the MEMS implementation. *Microelectronics Journal* 42: 277-282.
- Hajhosseini M and Rafeeyan M. (2016) Modeling and analysis of piezoelectric beam with periodically variable cross-sections for vibration energy harvesting. *Applied Mathematics and Mechanics* 37: 1053-1066.
- Halim MA, Kim DH and Park JY. (2016) Low Frequency Vibration Energy Harvester Using Stopper-Engaged Dynamic Magnifier for Increased Power and Wide Bandwidth. *Journal of Electrical Engineering and Technology* 11: 707-714.
- Halim MA and Park JY. (2014) Theoretical modeling and analysis of mechanical impact driven and frequency up-converted piezoelectric energy harvester for low-frequency and wide-bandwidth operation. *Sensors and Actuators A: Physical* 208: 56-65.
- Hu G, Tang L and Das R. (2017) An impact-engaged two-degrees-of-freedom Piezoelectric Energy Harvester for Wideband Operation. *Procedia Engineering* 173: 1463-1470.
- Hu GB, Tang LH, Das R, et al. (2018) A two-degree-of-freedom piezoelectric energy harvester with stoppers for achieving enhanced performance. *International Journal of Mechanical Sciences* 149: 500-507.
- Jiang WA, Chen LQ and Ding H. (2016) Internal resonance in axially loaded beam energy harvesters with an oscillator to enhance the bandwidth. *Nonlinear Dynamics* 85: 2507-2520.
- Kim KB, Nahm S, Sung TH, et al. (2016) Increasing Energy-harvesting ability of piezoelectric unimorph cantilevers using Spring Supports. *Journal of the Korean Physical Society* 68: 1262-1266.
- Lai SK, Wang C and Zhang LH. (2019) A nonlinear multi-stable piezomagnetoelastic harvester array for low-intensity, low-frequency, and broadband vibrations. *Mechanical Systems and Signal Processing* 122: 87-102.
- Lan C, Qin W and Deng W. (2015) Energy harvesting by dynamic instability and internal resonance for piezoelectric beam. *Applied Physics Letters* 107: 093902.
- Lee S, Youn BD and Jung BC. (2009) Robust segment-type energy harvester and its application to a wireless sensor. *Smart Materials & Structures* 18: 095021.
- Liu D, Xu Y and Li JL. (2017a) Probabilistic response analysis of nonlinear vibration energy harvesting system driven by Gaussian colored noise. *Chaos Solitons & Fractals* 104: 806-812.
- Liu D, Xu Y and Li JL. (2017b) Randomly-disordered-periodic-induced chaos in a piezoelectric vibration energy harvester system with fractional-order physical properties. *Journal of Sound and Vibration* 399: 182-196.
- Liu S, Cheng Q, Zhao D, et al. (2016) Theoretical modeling and analysis of two-degree-of-freedom piezoelectric energy harvester with stopper. *Sensors and Actuators A: Physical* 245: 97-105.

- Lu Zq, Li K, Ding H, et al. (2019) Nonlinear energy harvesting based on a modified snap-through mechanism. *Applied Mathematics and Mechanics (English Edition)* 40: 167-180.
- Moss S, Barry A, Powlesland I, et al. (2010) A low profile vibro-impacting energy harvester with symmetrical stops. *Applied Physics Letters* 97: 234101.
- Sun S and Cao SQ. (2017) Analysis of chaos behaviors of a bistable piezoelectric cantilever power generation system by the second-order Melnikov function. *Acta Mechanica Sinica* 33: 200-207.
- Wang JL, Geng LF, Ding L, et al. (2020) The state-of-the-art review on energy harvesting from flow-induced vibrations. *Applied Energy* 267: 17.
- Wang JL, Tang LH, Zhao LY, et al. (2019) Efficiency investigation on energy harvesting from airflows in HVAC system based on galloping of isosceles triangle sectioned bluff bodies. *Energy* 172: 1066-1078.
- Xie Z, Kwuimy CAK, Wang T, et al. (2019) Theoretical analysis of an impact-bistable piezoelectric energy harvester. *European Physical Journal Plus* 134: 190.
- Xu M, Jin XL, Wang Y, et al. (2014) Stochastic averaging for nonlinear vibration energy harvesting system. *Nonlinear Dynamics* 78: 1451-1459.
- Yuan TC, Yang J and Chen LQ. (2018) Nonlinear dynamics of a circular piezoelectric plate for vibratory energy harvesting. *Communications in Nonlinear Science and Numerical Simulation* 59: 651-656.
- Zhao D, Liu S, Xu Q, et al. (2018a) Theoretical modeling and analysis of a 2-degree-of-freedom hybrid piezoelectric–electromagnetic vibration energy harvester with a driven beam. *Journal of Intelligent Material Systems and Structures* 29: 2465-2476.
- Zhao LC, Zou HX, Yan G, et al. (2018b) Arbitrary-directional broadband vibration energy harvesting using magnetically coupled flextensional transducers. *Smart Materials and Structures* 27: 095010.
- Zhou S, Cao J, Inman DJ, et al. (2015) Impact-induced high-energy orbits of nonlinear energy harvesters. *Applied Physics Letters* 106.
- Zhou S and Zuo L. (2018) Nonlinear dynamic analysis of asymmetric tristable energy harvesters for enhanced energy harvesting. *Communications in Nonlinear Science and Numerical Simulation* 61: 271-284.
- Zhou SX, Cao JY, Inman DJ, et al. (2014) Broadband tristable energy harvester: Modeling and experiment verification. *Applied Energy* 133: 33-39.
- Zou HX, Zhao LC, Gao QH, et al. (2019) Mechanical modulations for enhancing energy harvesting: Principles, methods and applications. *Applied Energy* 255: 113871.